ChemPubSoc Europe

DOI: 10.1002/chem.201504846

CHEMISTRY A European Journal Full Paper

Perovskites |*Hot Paper*|

Alkaline Earth Metal Zirconate Perovskites $MZrO_3$ ($M = Ba^{2+}$, Sr^{2+}, Ca^{2+}) Derived from Molecular Precursors and Doped with Eu^{3+} Ions

Anna Drąg-Jarząbek, Łukasz John, Rafał Petrus, Magdalena Kosińska-Klähn, and Piotr Sobota*[a]

Abstract: The effect of alkaline earth metal alkoxides on the protonation of zirconocene dichloride was investigated. This approach enabled the design of compounds with preset molecular structures for generating high-purity binary metal oxide perovskites $MZrO_3$ ($M = Ba^{2+}$, Sr^{2+}, Ca^{2+}). Single-source molecular precursors $[Ba_4Zr_2(\mu_6\text{-}O)(\mu_3,\eta^2\text{-}OR)_8(OR)_2(\eta^2\text{-}HOR)_2(HOR)_2Cl_4]$, $[Sr_4Zr_2(\mu_6\text{-}O)(\mu_3,\eta^2\text{-}OR)_8(OR)_2(HOR)_4Cl_4]$, $[Ca_4Zr_2(\mu_6\text{-}O)(\mu_3,\eta^2\text{-}OR)_8(OR)_2Cl_4]$, and $[Ca_6Zr_2(\mu_2,\eta^2\text{-}OR)_{12}(\mu\text{-}Cl)_2(\eta^2\text{-}HOR)_4Cl_6]\cdot 8\,CH_2Cl_2$ were prepared via elimination of the cyclopentadienyl ring from Cp_2ZrCl_2 as CpH in the presence of $M(OR)_2$ and alcohol ROH ($ROH = CH_3OCH_2CH_2OH$) as a source of protons. The resulting complexes were characterized by elemental analysis, IR and NMR spectroscopy, and single-crystal X-ray diffraction. The compounds were then thermally decomposed to $MCl_2/MZrO_3$ mixtures. Leaching of MCl_2 from the raw powder with deionized water produced highly pure perovskite-like oxide particles of 40–80 nm in size. Luminescence studies on Eu^{3+}-doped $MZrO_3$ revealed that the perovskites are attractive host lattices for potential applications in display technology.

Introduction

Among the numerous types of binary oxides, alkaline earth metal perovskite oxides with the formula $MM'O_3$ ($M = Ca^{2+}$, Sr^{2+}, Ba^{2+}; $M' = Ti^{4+}$, Zr^{4+}, Hf^{4+}) have attracted much research interest. Such interest is mainly due to the wide range of applications of alkaline earth metal perovskite oxide nanomaterials in the fields of energy storage and conversion,[1] imaging technologies,[2] and heterogeneous catalysis.[3] For instance, Nishi et al. reported the long-lasting phosphorescence of titanium-doped barium zirconate ($BaZrO_3$) perovskite, which was synthesized by a conventional solid-state reaction.[4] Such materials have attracted considerable attention owing to their application as safety indicators, emergency lighting, and luminous paints.[5] Diaz-Torres and co-workers studied the intense blue and red emissions from $BaZrO_3$ powders doped with Yb^{3+} and Tm^{3+} ions.[6] Such interesting properties can find applications in aerospace technology and related areas. Additionally, Eu^{3+}-doped $BaZrO_3$ has luminescence properties, which are typically exploited in UV white light-emitting diodes (LEDs).[7] Strontium zirconate ($SrZrO_3$) finds applications in the fields of electronic ceramics, superconductors, phosphors, and coating materials. For instance, Zhou et al. showed that $SrZrO_3$ doped with Eu^{3+} ions emits reddish orange light and can be used in display applications.[8] Among group 2 zirconates, the most promising are rare earth doped calcium zirconate ($CaZrO_3$) owing to its potential applications. Zhang et al. reported that Eu^{3+}-doped $CaZrO_3$ displays very strong luminescence and a pure red color, which are attractive attributes for applications in display technology.[9] Eu-doped calcium zirconates can also be applied as a red phosphors for white LEDs.[10,11] The above-discussed materials are only a handful of examples of their potential in industry-related applications.

Binary oxide (nano)materials can be prepared by diverse routes. However, most of the above-discussed metal oxides were obtained by conventional synthesis routes such as solid-state reactions, chemical coprecipitation, Pechini-type sol–gel methods, and chemical vapor deposition. The main problem associated with the use of solid-phase synthesis for preparing alkaline earth metal oxide nanomaterials is poor product reproducibility. This is due to the highly non-equilibrium nature of the considered systems and the different properties displayed by the different stable states present in the system. The main factors that influence structure formation include deviation from the stoichiometry, introduction of chemical impurities, for example, by milling and high-temperature firing, undesirable phase formation, large grain sizes, poor chemical homogeneity, and expensive equipment requirements.[12]

We recently showed that reactions of multimetal components and their transformation into a complex product by a single-step synthesis route are very attractive for preparing

[a] *Dr. A. Drąg-Jarząbek, Dr. Ł. John, Dr. R. Petrus, M. Kosińska-Klähn, Prof. Dr. P. Sobota*
Faculty of Chemistry
University of Wrocław
14 F. Joliot-Curie, 50-383 Wrocław (Poland)
E-mail: piotr.sobota@chem.uni.wroc.pl

*Supporting information for this article (^1H and ^{13}C NMR spectra, core geometries for **1**, **2** and **4**, and XRD data) is available on the WWW under http://dx.doi.org/10.1002/chem.201504846.*

binary oxide nanomaterials.[13–18] Such heterometallic compounds with atypical combinations of elements have a fixed metal stoichiometry at the molecular level.[15] Thus, the composition of the oxide products after thermolysis can be easily predicted from the ratio of the metals. In this case, after thermal decomposition, which occurs at much lower temperatures compared with those employed in conventional approaches, binary host matrices for lanthanide ions can easily form. For instance, the phase-pure $BaHfO_3$ nanopowder obtained at 800 °C from $[Ba_4Hf_2(\mu_6\text{-}O)(\mu_3,\eta^2\text{-}OR)_8(OR)_2(\eta^2\text{-}ROH)_4Cl_4]$ (ROH = $CH_3OCH_2CH_2OH$) is an attractive host lattice for Eu^{3+} ions,[16] which are considerably more effective than the phosphors currently used in radiology and computed tomography. The number of structurally characterized heterometallic molecular precursors of heavier alkaline-earth metals is relatively small and includes some alkoxo (including both alkoxo and aryloxo metal complexes), alkoxo hydride, and alkoxo organometallic complexes. Studies on the preparation of calcium zirconate alkoxides are limited to four precursor compounds, of which three of were synthesized by us. However, none of these complexes contained metals in the 1:1 ratio that is desirable for perovskite phases. Accordingly, we aimed to prepare simple, stable, and readily thermally decomposable alkoxide precursors with strictly defined molecular structures for use in the synthesis of group 2 perovskite zirconates that can be efficiently synthesized by common synthetic approaches.[17,19,20] In this paper, we report the high-yield synthesis of new single-source precursors for the preparation of highly phase pure $MZrO_3$ perovskites as host matrices for various lanthanide ions for subsequent applications as luminescent materials. Here we show that using organometallic and alkoxide compounds in the synthesis of molecular precursors for complex oxide materials is extremely effective. On the other hand, working with such compounds, in many cases, is cumbersome due to their sensitivity to air and moisture. From this perspective, zirconocene dichloride is an air-stable organometallic compound and its use is much more convenient.

Results and Discussion

Syntheses and structures

We focused on designing precursors with well-defined metal elements with stoichiometry suitable for obtaining highly pure perovskite-like binary oxides. Thus, the selection of appropriate ligands that would positively influence the solubilities and crystallization abilities of particular compounds was essential. Accordingly, we investigated 2-methoxyethanol as potential ligand. It contains two donor atoms, that is, an alkoxy oxygen atom and an ether oxygen atom, separated by two carbon atoms. These donor atoms allow the ligand to act as a chelating agent and additionally to be tethered in μ-η^2 mode to readily generate multinuclear metal species. In our synthetic strategy for the preparation of perovskite precursors, organometallic species played a key role in generating precisely defined stoichiometries of metal elements on the molecular level. For instance, group 4 metallocene dichlorides $[Cp_2MCl_2]$ (M = Ti^{4+}, Zr^{4+}, Hf^{4+}) are attractive and cheap substrates for use in such reactions. However, the ability of Cp to act as a leaving group in metallocenes has been neglected, and its wider applications remain unknown.

The treatment of $[Cp_2ZrCl_2]$ with two equivalents of barium metal and an excess of 2-methoxyethanol in toluene at room temperature gave free CpH and colorless cyclopentadienyl-free $[Ba_4Zr_2(\mu_6\text{-}O)(\mu_3,\eta^2\text{-}OR)_8(OR)_2(\eta^2\text{-}HOR)_2(HOR)_2Cl_4]$ (**1**, 82%, ROH = $CH_3OCH_2CH_2OH$). Compound **1** was obtained as a mixture of two crystalline forms that differed in the arrangements of alcohol ligands around the Ba1 atoms. Furthermore, when strontium or calcium metal was used instead of barium, $[Sr_4Zr_2(\mu_6\text{-}O)(\mu_3,\eta^2\text{-}OR)_8(OR)_2(HOR)_4Cl_4]$ (**2**, 59%) and $[Ca_4Zr_2(\mu_6\text{-}O)(\mu_3,\eta^2\text{-}OR)_8(OR)_2Cl_4]$ (**3**, 71%) formed, respectively (Scheme 1).

Scheme 1. Synthesis of **1**–**3**.

In these reactions, zirconocene dichloride underwent transformation involving chloride ion loss, coordination of an alcohol to the Zr center, followed by total replacement of Cp groups with 2-methoxyethoxide anions. Thus, these processes bestowed proton functionalities necessary for cyclopentadiene evolution. The release of free CpH during the reaction was monitored by ^{1}H NMR spectroscopy and GC-MS. $M(OR)_2$ that was generated in situ during the reaction bound to the chloride anions, thereby shifting the chloride dissociation equilibrium to the right and initiating a multistage process that proceeded through intermolecular detachment of cyclopentadiene from the metal site, which consequently led to the formation of heterometallic clusters **1**–**4**.[16] The resulting complexes were characterized by elemental analysis and FTIR and NMR spectroscopy. In the case of **1**, **2**, and **4**, single-crystal XRD analysis was also performed.

The single-crystal XRD data showed that **1** and **2** are centrosymmetric hexanuclear clusters with a $M_4Zr_2(\mu_6\text{-}O)(\mu_3\text{-}O)_8$ central core structure, where M = Ba^{2+} and Sr^{2+}, respectively (Figures 1 and 2). The six metal ions form an octahedron with one interstitial μ_6-O atom and eight μ_3-O bridges. During the preparation of alkoxometal compounds, the formation of "lone" oxo O^{2-} groups in the products is not uncommon, and has been extensively reported in the literature.[21] The Zr ions have six-coordinate distorted octahedral coordination environments with O_6 donor sets, whereas the alkaline earth metal ions are surrounded by O_8Cl (for Sr and Ba) or O_9Cl (for Ba) donor atoms. The characteristic interatomic distances in the heterogeneous cores of clusters **1**, **2**, and **4** are listed in Table S2 (see Supporting Information).

Compound **1** is composed of a mixture of two crystalline forms, which were characterized by XRD. Both forms crystallize in triclinic space group $P\bar{1}$ with two different unit-cell parameters (for details see Table S2 in the Supporting Information). The structure of **1**′ differed from that of **1** only in the coordina-

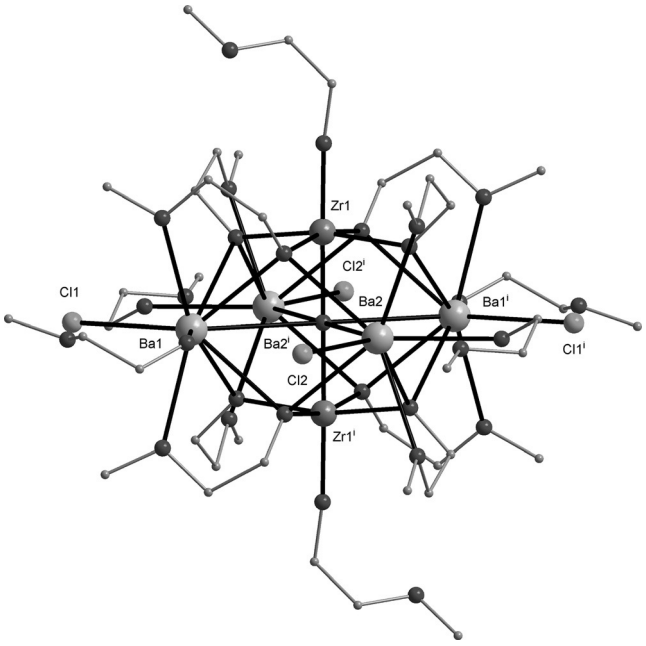

Figure 1. Molecular structure of **1**. The second disordered counterpart of the alkoxyl group and hydrogen atoms are omitted for clarity. Symmetry code: i) $-x+1$, $-y+1$, $-z+1$.

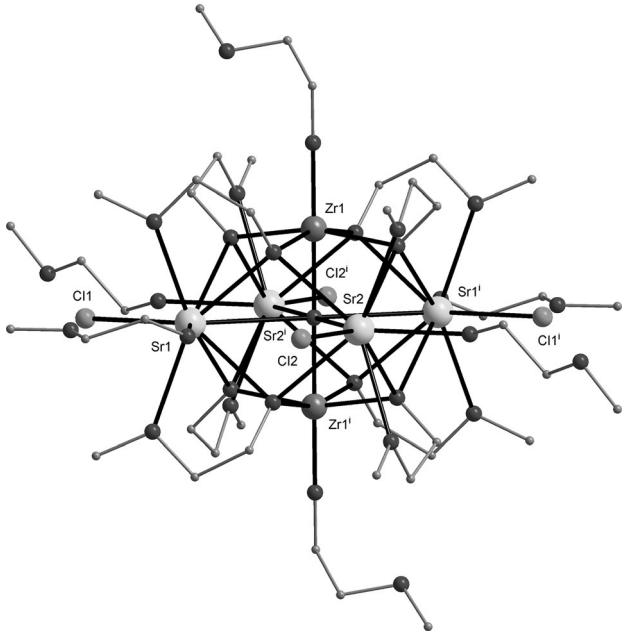

Figure 2. Molecular structure of **2**. The second disordered counterpart of the alkoxyl group and hydrogen atoms are omitted for clarity. Symmetry code: i) $-x+1$, $-y+1$, $-z+1$.

tion number around the Ba1 atom. This difference was attributed to the different coordinating modes of ROH molecules. Moreover, when the synthesis of **1** was performed in ethanol/2-methoxyethanol, the bis-ethanol-solvated form of **1** (**1**''·2 EtOH) was obtained, which contains an alcohol molecule at the Ba2 site, occupied partly by EtOH and $CH_3OCH_2CH_2OH$ in the ratio of 0.5:0.5.

Crystallization of compound **3** from toluene and toluene/*n*-hexane was attempted, but without any success. The composition and structure of **3** were confirmed by physicochemical methods including elemental analysis and FTIR, ^{1}H NMR, and ^{13}C NMR spectroscopy.

The stoichiometry of the reagents and solvents used for the crystallization of the heterometallic compounds seemed essential for the synthesis of calcium zirconium complexes. Recently, we showed that $[Cp_2ZrCl_2]$ undergoes transformation involving the loss of only one Cp ring after treatment with calcium 2-methoxyethoxide in methoxyethanol/toluene/dichloromethane, which results in $[Cp_2Ca_4Zr_2(\mu_3,\eta^2\text{-}OR)_4(\mu,\eta^2\text{-}OR)_4(\mu_4\text{-}Cl)(\mu\text{-}Cl)_3Cl_2]\cdot 1.5\,CH_2Cl_2$.[13] Subsequently, when $[Cp_2ZrCl_2]$ was treated with Ca in the presence of ROH and toluene and the product recrystallized from CH_2Cl_2, $[Ca_6Zr_2(\mu_2,\eta^2\text{-}OR)_{12}(\mu\text{-}Cl)_2(\eta^2\text{-}HOR)_4Cl_6]\cdot 8\,CH_2Cl_2$ (**4**·8 CH_2Cl_2, 24%) was obtained. We postulate that the second product is a zirconium alkoxide complex that remains in solution.

Complex **4** is an octanuclear calcium zirconium chloro alkoxide based on a central $Ca_6Zr_2(\mu_2\text{-}O)_{12}(\mu_2\text{-}Cl)_2$ core. Formally, **4** is a centrosymmetric cluster consisting of two $\{ZrCa_3(\mu_2,\eta^2\text{-}OR)_6(\eta^2\text{-}OR)_2(\mu\text{-}Cl)Cl_3\}$ moieties bridged by two μ_2-chlorido ligands (Figure 3). The Ca atoms are seven-coordinate with O_6Cl and O_4Cl_3 donor sets in a distorted pentagonal-bipyramidal geometry. In contrast, the zirconium ions form six-coordinate distorted octahedra with O_6 donor sets.

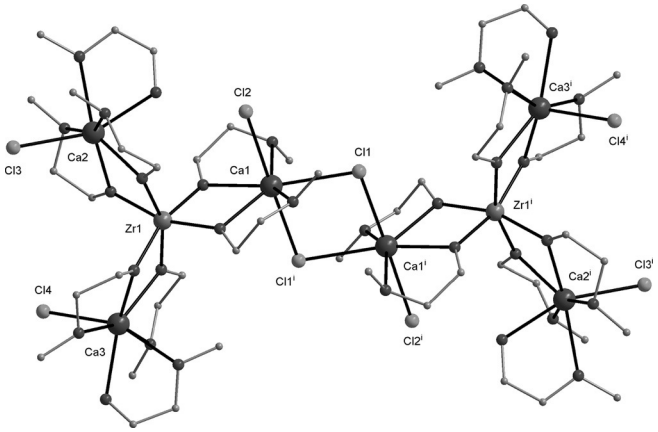

Figure 3. Molecular structure of **4**. The second disordered counterparts of ligands, solvent molecules, and hydrogen atoms are omitted for clarity. Symmetry code: i) $-x+1$, $-y+1$, $-z+1$.

Thermal decomposition of 1–3

Complexes **1**–**3** were selected as the most promising molecular precursors for the preparation of the corresponding double oxides. In contrast, **4** was excluded because its use led to the formation of various oxide phases, which were difficult to identify. The thermal decomposition of clusters **1**–**3** was investigated by thermogravimetric/differential thermal analysis (TG/DTA) in air. Heterometallic alkoxide complexes **1**–**3** underwent multistep transformations on heating from room temperature to 600 °C (Figure 4).

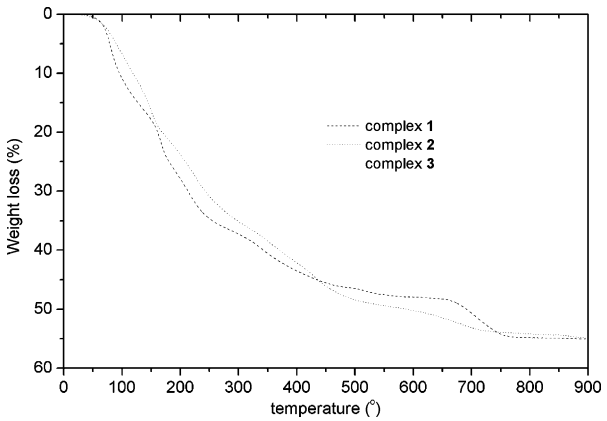

Figure 4. TGA curves of **1**–**3**.

The weight losses observed in the TGA curves in the range 20–500 °C were attributed to the pyrolysis of organic ligands. The subsequent weight losses in the temperature range of 600–800 °C were attributed to the decomposition of residual organic components from a mixture of MCl_2 and $MZrO_3$ in a 1:1 molar ratio (Table 1). The key factor in preparing pure perovskite-type oxides is to choose appropriate thermal decomposition conditions, by taking into consideration the melting points of the corresponding chlorides: $BaCl_2$ 962 °C, $SrCl_2$ 874 °C, $CaCl_2$ 772 °C.[22] Thus, in a typical procedure, **1** was thermally decomposed at 900 °C, and **2** and **3** were decomposed at 850 and 750 °C, respectively. The thermal decomposition of **1**–**3** generated a mixture of two compounds, $MZrO_3$ and MCl_2 (M = Ba^{2+}, Sr^{2+}, Ca^{2+}), which could be easily separated by their different solubilities in water. Subsequently, the raw powders were leached with deionized water, and then dried in an oven at 120 °C for 1 h. The crystal structures of pure barium zirconate and strontium zirconate were confirmed by XRD (Figure 5 and Figure 6).

Table 1. Thermolysis data of **1**–**3**. Experimental (TGA) and calculated weight losses for the mixture of $MZrO_3$ and MCl_2.

Complex	T_{decomp} [°C]	Exptl weight loss [%]	Calcd weight loss [%]
1	900	49.62	50.15
2	850	54.92	55.86
3	750	53.19	53.61

Conversely, $CaZrO_3$ was obtained by thermal decomposition of complex **3** at 750 °C (1 h) under air. The raw powder was also leached with deionized water and subsequently heat-treated at 900 °C under the same conditions as those used for barium and strontium zirconates. The phase purity of the final residue was confirmed by powder XRD (Figure 7).

The morphology and chemical composition of the microcrystalline perovskite zirconates were investigated by SEM/energy-dispersive X-ray spectroscopy (EDS) and TEM-EDS (Figures 8 and 9). Carbon, hydrogen, and chlorine contamination was examined by elemental analysis and FTIR spectroscopy.

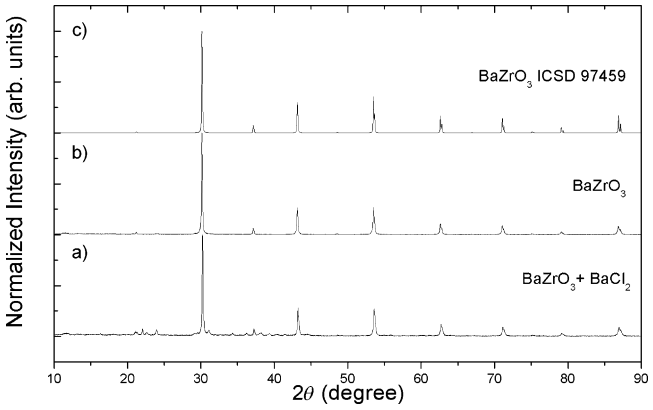

Figure 5. Powder XRD patterns of a) a mixture of $BaCl_2$ and $BaZrO_3$, b) $BaZrO_3$, and c) $BaZrO_3$ (ICSD 97459).

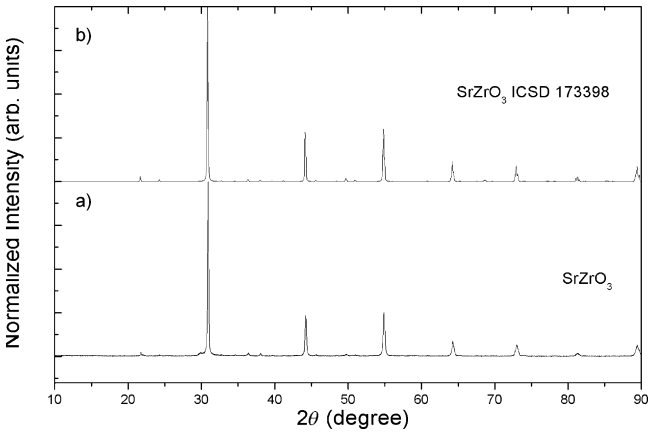

Figure 6. Powder XRD patterns of a) $SrZrO_3$ and b) $SrZrO_3$ (ICSD 173398).

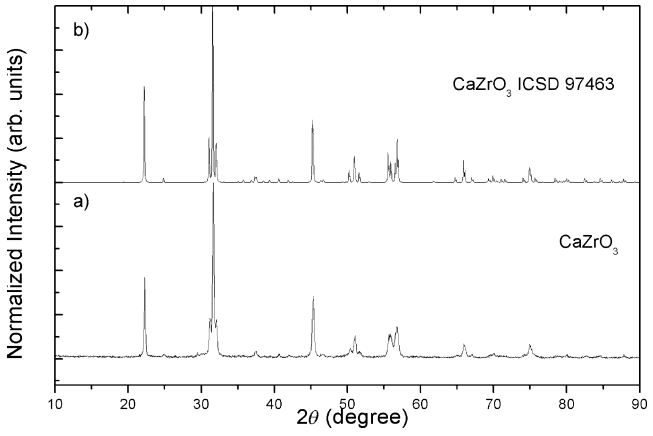

Figure 7. Powder XRD patterns of a) $CaZrO_3$ and b) $CaZrO_3$ (ICSD 97463).

Luminescence studies on group 2 zirconates doped with Eu^{3+} ions

Figure 10 shows the XRD patterns of the $MZrO_3$ powders doped with Eu^{3+}, denoted $M_{0.97}ZrO_3:Eu_{0.03}$ (M = Ba, Sr, Ca). The positions of the diffraction peaks agreed with those observed

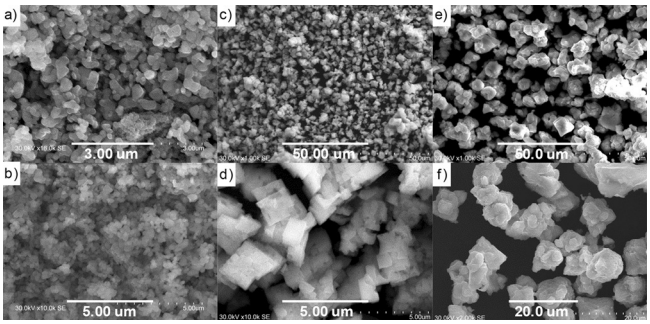

Figure 8. SEM images of a), b) $BaZrO_3$, c), d) $SrZrO_3$, and e), f) $CaZrO_3$.

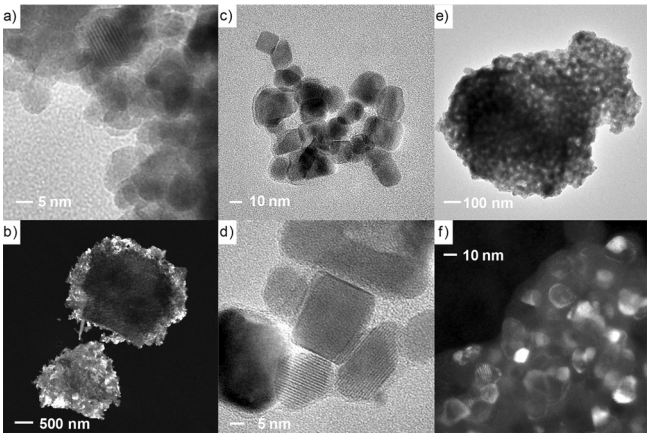

Figure 9. TEM images of a), b) $BaZrO_3$, c), d) $SrZrO_3$, and e), f) $CaZrO_3$.

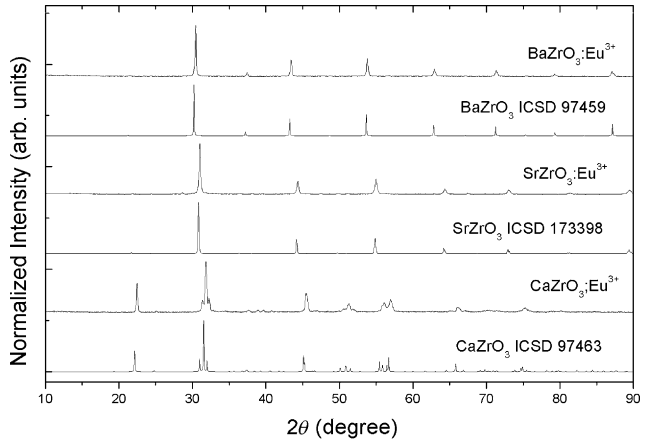

Figure 10. Powder XRD patterns of $MZrO_3:Eu^{3+}$ (M = Ba, Sr, Ca) derived from molecular precursors. The reference patterns are also shown for comparison.

in the standard XRD patterns. Thus, doping with Eu^{3+} ions did not change the lattice of the powder, since additional peaks of Eu_2O_3 and $Eu_2Zr_2O_7$ were not detected in the sample.

Figure 11 shows the excitation ($\lambda_{em} = 595$ nm) and emission ($\lambda_{exc} = 265$ nm) spectra of $Ba_{0.97}ZrO_3:Eu_{0.3}$. The excitation spectrum (Figure 11 a) showed a peak at 235 nm, which was attributed to the host lattice absorption, a wide band with strong intensity at 265 nm, which was attributed to a charge-transfer

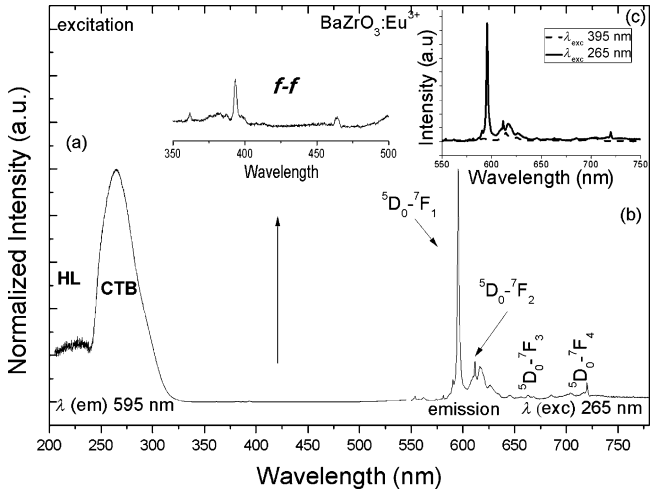

Figure 11. Photoluminescence spectra of $BaZrO_3:Eu^{3+}$ (3%). a) excitation spectrum $\lambda_{em} = 595$ nm, b) emission spectrum $\lambda_{exc} = 265$ nm, c) comparison of emission spectra excited with $\lambda_{exc} = 265$ nm and $\lambda_{exc} = 395$ nm.

band ($O^{2-} \rightarrow Eu^{3+}$), and very weak f–f transition lines in the range of 350–550 nm.

The emission spectrum (Figure 11 b) showed a series of narrow bands corresponding to the transitions of $^5D_0 \rightarrow {}^7F_J$ ($J = 1, 2, 3, 4$) levels of Eu^{3+} ions. The strongest peak was observed at 595 nm and was assigned to the magnetic dipole transition $^5D_0 \rightarrow {}^7F_1$. It is well known that luminescence lines of Eu^{3+} transitions are sensitive to the local environment of Eu^{3+} ions. The magnetic dipole transition $^5D_0 \rightarrow {}^7F_1$ is dominant when Eu^{3+} ions are located at a site of inversion symmetry; conversely, the electric dipole transition $^5D_0 \rightarrow {}^7F_2$ is dominant when Eu^{3+} ions occupy a site of noninversion symmetry.[7–11,16] Thus, it could be deduced that Eu^{3+} ions occupied the symmetry site in $BaZrO_3$ phosphor. Owing to the difference in radii among Eu^{3+} (0.095 nm), Ba^{2+} (0.135 nm), and Zr^{4+} (0.072 nm), Eu^{3+} ions were expected to occupy the Zr^{4+} sites in the $BaZrO_3$ lattice.[7] Figure 11 c shows that the emission on excitation at $\lambda_{exc} = 265$ nm (charge-transfer band (CTB) $O^{2-} \rightarrow Eu^{3+}$) was more intense than that on excitation at $\lambda_{exc} = 395$ nm ($^7F_0 \rightarrow {}^5L_6$ of Eu^{3+}). The considerably weak lines of f–f transitions in the excitation spectrum and the low intensity of emission on direct Eu^{3+} excitation suggest that a high quantum efficiency of Eu^{3+} luminescence excitation originates from charge transfer between O^{2-} and Eu^{3+} ions.[8]

Figure 12 shows the excitation ($\lambda_{em} = 615$ nm) and emission ($\lambda_{exc} = 393$ nm) spectra of $Sr_{0.97}ZrO_3:Eu_{0.3}$. The excitation spectrum (Figure 12 a, solid line) shows a broad peak centered at 260 nm, which is ascribed to the CTB originating from electron transfer from an oxygen ion (2p orbital) to an europium ion (empty 4f orbital). In the 350–550 nm range, sharp lines, ascribed to 4f–4f Eu^{3+} transitions, were observed. The emission spectrum (Figure 12 b, dashed line) features a series of narrow lines, corresponding to $^5D_0 \rightarrow {}^7F_J$ ($J = 0, 1, 2, 3, 4$) emission of Eu^{3+} ions.

The excitation ($\lambda_{em} = 594$ nm) and two emission spectra ($\lambda_{exc} = 250$ and 295 nm) of $Sr_{0.97}ZrO_3:Eu_{0.3}$ phosphor are shown

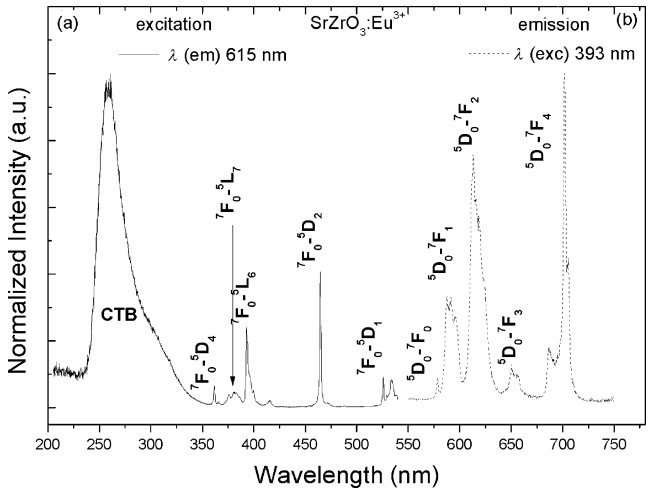

Figure 12. Photoluminescence spectra of $SrZrO_3$:Eu^{3+} (3%). a) excitation spectrum λ_{em} = 615 nm, b) emission spectrum λ_{exc} = 393 nm.

in Figure 13. Compared with the spectra in Figure 12, the intensity of the excitation band centered at 250 nm is similar. However, the f–f transition lines were significantly weaker (Figure 13a, solid line). Figure 13b(dashed line) shows that the emission intensity of the $^5D_0 \rightarrow {}^7F_1$ transition (594 nm) is much stronger than that of the $^5D_0 \rightarrow {}^7F_2$ transition (614 nm) on excitation with 250 nm light. Conversely, the opposite trend was observed on excitation with 295 nm light (solid line). The $^5D_0 \rightarrow {}^7F_2$ transition is regarded as an efficient probe to detect inversion environmental symmetry around Eu^{3+} ions in the lattice.

Because the ratio between the magnetic (594 nm) and electric dipole transition (615 nm) changed on different excitations, and owing to the different sizes of Sr^{2+} (0.118 nm), Zr^{4+} (0.072 nm), and Eu^{3+} (0.095 nm), it is believed that Eu^{3+} ions may in part occupy the Sr^{2+} site and in part the Zr^{4+} site in the host lattice. Information about the local environment of

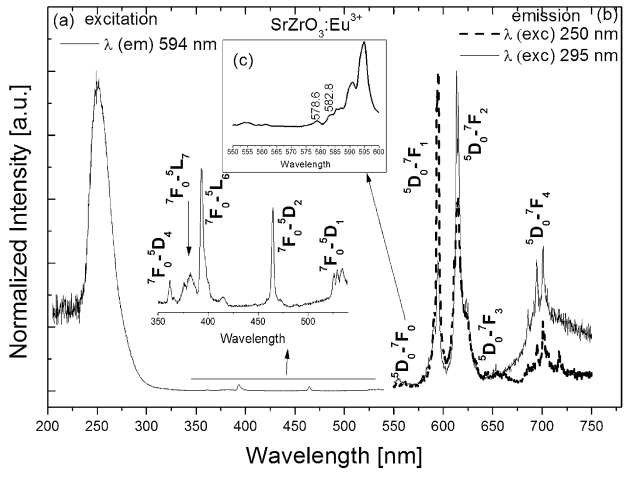

Figure 13. Photoluminescence spectra of $SrZrO_3$:Eu^{3+} (3%). a) excitation spectrum λ_{em} = 594 nm, b) emission spectrum λ_{exc} = 250 nm (dashed line) and λ_{exc} = 295 nm (solid line), c) inset of emission from 550–600 nm wavelength region excited with λ_{exc} = 295 nm.

Eu^{3+} ions can also be obtained from the splitting number of $^5D_0 \rightarrow {}^7F_J$ transitions and the site of symmetry of the Eu^{3+} ion, whereby the maximum number of lines is limited to $2J+1$ for each site.[8]

The inset of Figure 13c shows two lines associated with $^5D_0 \rightarrow {}^7F_0$ transition, which thus exceeds the maximum permissible number of lines for this transition. Therefore, this indicates that Eu^{3+} ions occupy two different sites in the $SrZrO_3$ lattice.[8]

Figure 14 shows the photoluminescence spectra of $Ca_{0.97}ZrO_3$:$Eu_{0.03}$. The excitation spectrum (Figure 14a, solid line) was obtained by monitoring the $^5D_0 \rightarrow {}^7F_2$ transition of Eu^{3+}. The spectrum showed a wide band in the range of 230–320 nm, peaking at 263 nm, and a series of narrow peaks in the region of 350–550 nm. The observed peaks were assigned to the CTB originating from electron transfer between O^{2-} and Eu^{3+} ions and f–f transitions, respectively.

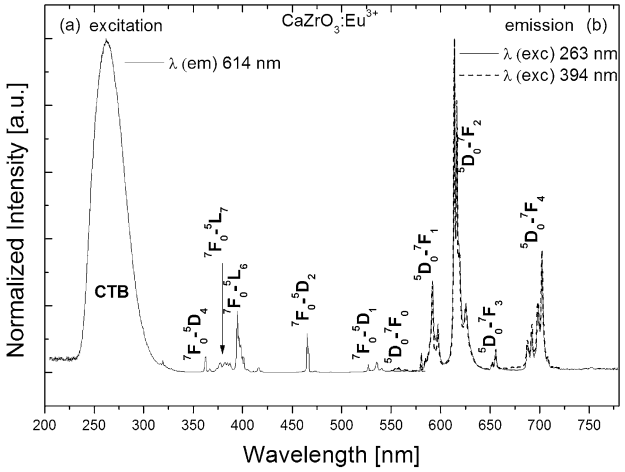

Figure 14. Photoluminescence spectra of $CaZrO_3$:Eu^{3+} (3%).

The most intense f–f excitation peak was located at 394 nm and attributed to the $^7F_0 \rightarrow {}^5L_6$ transition. In contrast, the emission spectra (Figure 14b, dashed and solid lines) displayed characteristic sharp lines at 590, 592, 614, 655, and 702 nm corresponding to $^5D_0 \rightarrow {}^7F_J$ (J = 0, 1, 2, 3, 4) transitions of Eu^{3+}, respectively. Both spectra, excited at 263 and 394 nm, featured similar shapes and peak intensities. As the intensity of the emission line assigned to the electric dipole transition $^5D_0 \rightarrow {}^7F_2$ (614 nm) of Eu^{3+} was much stronger than that of the magnetic dipole transition $^5D_0 \rightarrow {}^7F_1$ (592 nm), Eu^{3+} ions could occupy the lattice sites without inversion symmetry. The similar ionic radii of Eu^{3+} (0.095 nm) and Ca^{2+} (0.099 nm) suggest that Eu^{3+} could occupy Ca^{2+} sites in the host lattice.[11] The $CaZrO_3$ lattice has an orthorhombic-distorted perovskite structure, whereby the point symmetry is C_1 with no inversion center at the Ca site. Hence, Eu^{3+} ions are positioned in an asymmetrical site when they substitute for Ca^{2+} sites.[10]

Figure 15 shows the emission spectra of $MZrO_3$:Eu^{3+} (M = Ca, Sr, Ba) at excitation wavelengths of 263, 250, and 265 nm. The luminescence intensity ratio of $^5D_0 \rightarrow {}^7F_2$ to $^5D_0 \rightarrow {}^7F_1$ was used as a symmetry probe around Eu^{3+} in the host. This ratio

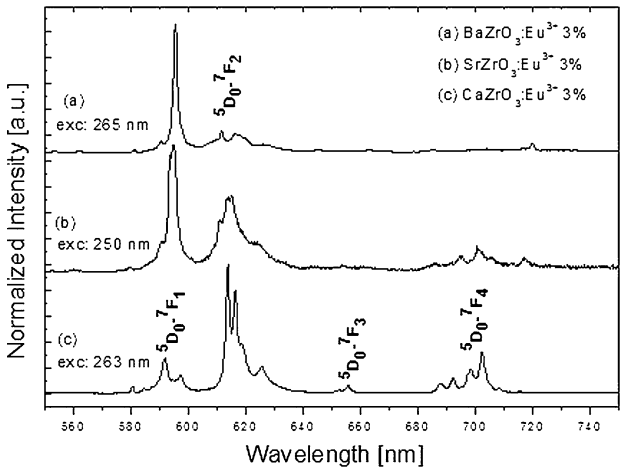

Figure 15. Excitation spectra of $MZrO_3:Eu^{3+}$ (M = Ba, Sr, Ca). a) $BaZrO_3:Eu^{3+}$, b) $SrZrO_3:Eu^{3+}$, c) $CaZrO_3:Eu^{3+}$.

decreased with increasing radius of the group 2 metals. Moreover, the number of emission lines in calcium zirconate was higher than that in the two other materials. The latter observation also reflects that the symmetry around Eu^{3+} is lower in this sample. Additionally, $CaZrO_3:Eu^{3+}$ displayed considerably stronger luminescence than $BaZrO_3:Eu^{3+}$ and $SrZrO_3:Eu^{3+}$, which suggests that the calcium zirconate lattice is the most suitable for doping with Eu^{3+} ions, and hence the most promising candidate for white LED applications.

Figure 16 shows the excitation spectra of $MZrO_3:Eu^{3+}$ (Ca, Sr, Ba), from which the most intensive emission line could be observed. The emission wavelength was fixed at 614 nm for $CaZrO_3$, 594 nm for $SrZrO_3$, and 595 nm for $BaZrO_3$. The measured spectra showed common features, namely, a broad band, which was attributed to europium–oxygen charge-transfer interaction, and weak sharp lines in the 350–500 nm region, which were assigned to f–f transitions of Eu^{3+}. The positions of the CTBs were different in the different matrices, with peaks at 263, 250, and 265 nm for $CaZrO_3:Eu^{3+}$, $SrZrO_3:Eu^{3+}$, and $BaZrO_3:Eu^{3+}$, respectively. Similar results were reported by Zhang et al.,[9] who attributed this phenomenon to the fact that the position of the CTB is closely related to covalence between O^{2-} and Eu^{3+}. The covalence decreases with increasing energy for electron transfer from O^{2-} to Eu^{3+} and is mainly influenced by the Zr–O bond in the bond structure of Eu^{3+}–O^{2-}–Zr^{4+}. The octahedron, with Zr^{4+} in the center, tends to tilt because of the mismatch of the alkaline earth metal ions with the dodecahedral cavity in the crystal structure. This can induce a length change in the Zr–O bond. The $SrZrO_3$ phosphor has the shortest mean Zr–O bond length. Thus, Zr^{4+} can more strongly attract the electrons of O^{2-}, and hence electron transfer from O^{2-} to Eu^{3+} ions is more difficult. Hence, the CTB of Eu^{3+} in $SrZrO_3:Eu^{3+}$ was located at a short wavelength of 250 nm, whereas in $CaZrO_3:Eu^{3+}$ and $BaZrO_3:Eu^{3+}$, the band shifted to a longer-wavelength region and lower energy, that is, 263 and 265 nm, respectively.

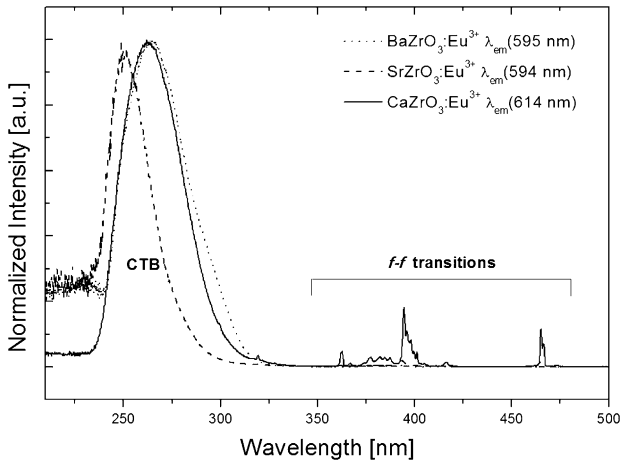

Figure 16. Emission spectra of $MZrO_3:Eu^{3+}$ (M = Ba, Sr, Ca).

Conclusion

We have presented a simple, high-yield synthetic route for the easily scaled up preparation of well-defined, single-source precursors for preparing alkaline earth metal zirconate perovskites $MZrO_3$ ($M = Ba^{2+}$, Sr^{2+}, and Ca^{2+}). The precursor compounds were prepared by simple elimination of the Cp^- anion from the zirconocene dichloride as cyclopentadiene in the presence of $M(OR)_2$, by using 2-methoxyethanol as a source of protons. Under thermal treatment, the resulting coordination complexes decomposed to a mixture of MCl_2 and group 2 zirconate perovskites. Pure perovskites were separated from the chlorides by simple MCl_2 leaching from the raw powder with deionized water. The resulting particles were 40–80 nm in size. Thus, these studies demonstrated that using metal alkoxides and their organometallic derivatives is viable to synthesize molecular precursors for the preparation of numerous metal oxide materials at lower temperatures than those typically used in conventional solid-state thermal routes involving carbonate/oxide mixtures. Subsequently, the synthesized oxides were doped with Eu^{3+} ions to produce luminescent materials. The $CaZrO_3:Eu^{3+}$ phosphor featured the highest luminescence intensity. On near-UV excitation (396 nm), the phosphor showed bright red emission corresponding to the $^5D_0 \rightarrow {}^7F_2$ transition of Eu^{3+}. Therefore, it is considered to be the most promising candidate for application in trichromatic white LEDs.[9,11]

Experimental Section

General procedures

All reactions were performed under N_2 atmosphere by using standard Schlenk and vacuum-line techniques. The commercially available solvents were purified by conventional methods. Toluene and hexane were distilled from Na; CH_2Cl_2 was distilled from P_2O_5; and THF was distilled from Na/benzophenone. Barium (pieces, 99%), strontium (granules, 99%), calcium (pieces, 99%), $[Cp_2ZrCl_2]$ (powder, 98%), 2-methoxyethanol (anhydrous liquid, 99.8%), and Eu_2O_3 (powder 99.9%) were purchased from Aldrich and used without further purification. **Caution!** 2-Methoxyethanol is classified as highly poisonous and its use is restricted.

Methods

Microanalyses were conducted with a 2400 CHNS Vario EL III (Elementar) elemental analyzer. The concentrations of the metal ions were determined by inductively coupled plasma atomic emission spectrometry (ICP-AES) with an ARL 3410 sequential spectrometer (Fisons Instruments). FTIR spectra were recorded as Nujol mulls with a Bruker 66s FTIR spectrometer. NMR spectroscopy was performed with a Bruker ADVANCE 500 MHz spectrometer. Mass spectrometry was performed with a MicrOTOF-Q ESI mass spectrometer (Bruker), and GC-MS was conducted with a gas chromatograph equipped with a mass detector (Hewlett Packard, Model HP 5971A). TGA-DTA was performed under air with a SETSYS 16/18 system (SETARAM) at a heating rate of 10 °C min^{-1}. Thermal decomposition was performed in a NT 1313 furnace equipped with a KXP3+ thermostat (NEOTHERM). Samples were heated in atmospheric air. The thermolysis products were characterized by powder XRD with a Bruker D8 ADVANCE diffractometer, equipped with a copper lamp ($\lambda(Cu_{K\alpha})=1.5418$ Å). The measurements were performed in the range of $2\theta=10$–90° in 2θ steps of 0.016° with a counting time of 0.3 s. The morphology of the prepared powders was examined by high-resolution TEM and SEM. TEM analysis was conducted with a FEI Tecnai G^2 20 X-TWIN microscope equipped with an EDS microanalyzer and operating at 200 kV (resolution 0.25 nm). SEM analysis was performed with a Hitachi S-3400N microscope equipped with a Thermo Noran System SIX EDS system. Photoluminescence spectra were recorded with an FSL920 spectrofluorometer (Edinburgh Instruments) equipped with a 450 W Xe lamp and photomultiplier tube, operating in the range of 185–870 nm. The luminescence spectra were recorded with a resolution of 0.2 nm. XRD data were collected at 100 K by using a KUMA KM4 CCD κ-geometry diffractometer (ω scan technique). The experimental details and the crystal data are given in Table S1 (Supporting Information). The structures were solved by direct methods and refined by full-matrix least-squares techniques on F^2 by using the SHELXTL package. Non-hydrogen atoms were refined with anisotropic thermal parameters. All hydrogen atoms were positioned geometrically and added to the structure factor calculations, but were not refined. The molecular graphics were created with Diamond, version 3.1e. CCDC 1435943 (**1**), 1435944 (**1′**), 1435945 (**1″**), 1435946 (**2**), and 1435947 (**4**) contain the supplementary crystallographic data for this paper. These data are provided free of charge by The Cambridge Crystallographic Data Centre

Synthesis

$[Ba_4Zr_2(\mu_6\text{-}O)(\mu_3,\eta^2\text{-}OR)_8(OR)_2(\eta^2\text{-}HOR)_2(HOR)_2Cl_4]$ (1) and $[Ba_4Zr_2(\mu_6\text{-}O)(\mu_3,\eta^2\text{-}OR)_8(OR)_2(\eta^2\text{-}HOR)_4Cl_4]$ (1′): A Schlenk flask was charged with $[Cp_2ZrCl_2]$ (1.00 g, 3.42 mmol), Ba metal (1.24 g, 9.03 mmol), 2-methoxyethanol (20 mL, 19.30 g, 0.25 mol), and toluene (20 mL). **Caution**! Barium undergoes an extremely rapid and exothermic reaction. The mixture was vigorously stirred until all metal was consumed (typically within 2 h). The resulting light brown solution was filtered, concentrated under vacuum to 20 mL, and left to crystallize at room temperature. After a few hours, colorless crystals of **1** were collected, washed with *n*-hexane (3× 5 mL), and dried under vacuum. The filtrate was concentrated to 10 mL and subsequently produced a crystalline material after standing overnight. Overall yield: 2.72 g (1.40 mmol, 82%); ^{1}H NMR (500 MHz, $CDCl_3$, 298 K): $\delta=4.15$ (brs; OCH'_2), 4.02 (t, J(H,H)=5 Hz; OCH''_2,), 3.75 (t, J(H,H)=5 Hz; OCH'''_2), 3.64 (brs; CH'_2O), 3.55 (s; OCH'_3), 3.52 (s; OCH'''_3), 3.51–3.50 (m; CH'''_2O), 3.34 (t, J(H,H)= 5 Hz; CH''_2O), 3.28 ppm (s; OCH''_3); $^{13}C\{^1H\}$ NMR (500 MHz, $CDCl_3$, 298 K): $\delta=77.36$, 76.12, 73.83 (CH_2O), 67.35, 65.04, 60.99 (OCH_2), 59.70, 59.62, 58.55 ppm (OCH_3); IR (Nujol): $\tilde{\nu}=3478$ (w), 3133 (s), 2924 (vs), 2854 (vs), 2765 (w), 2714 (w), 1619 (vw), 1456 (s), 1377 (m), 1365 (m), 1344 (w), 1289 (vw), 1246 (m), 1200 (w), 1163 (s), 1116 (s), 1068 (s), 1023 (s), 928 (vw), 898 (s), 834 (m), 802 (w), 712 (m), 687 (s), 552 (m), 459 (m), 413 (s), 374 (s), 318 cm^{-1} (m); MS ($CHCl_3$) found: $m/z=1604.8$ $[Ba_4Zr_2(\mu_6\text{-}O)(\mu_3,\eta^2\text{-}OR)_8(\eta\text{-}OR)_2Cl_3]^+$; calcd: 1605.0; elemental analysis calcd (%) for $C_{42}H_{102}O_{29}Cl_4Ba_4Zr_2$: C 25.94, H 5.29, Cl 7.29, Ba 28.24, Zr 9.38; found: C 25.90, H 5.16, Cl 7.20, Ba 28.13, Zr 9.09.

In the crystalline form **1′**, the arrangement of $CH_3OCH_2CH_2OH$ ligands around the Ba1 atom in **1** is changed and the coordination number of the Ba1 center is increased from 9 to 10.

$[Ba_4Zr_2(\mu_6\text{-}O)(\mu_3,\eta^2\text{-}OR)_8(OR)_2(\eta^2\text{-}HOR)_2(HOR^*)_2Cl_4]\cdot 2\,EtOH$ (1″·2 EtOH) (R*OH = 0.5 EtOH/0.5 ROH): A Schlenk flask was charged with $[Cp_2ZrCl_2]$ (0.72 g, 2.46 mmol), Ba metal (0.68 g, 4.95 mmol), 2-methoxyethanol (5 mL, 4.82 g, 63.41 mmol), ethanol (10 mL, 7.89 g, 171.26 mmol), and THF (5 mL). **Caution!** Barium undergoes an extremely rapid and exothermic reaction. The mixture was vigorously stirred until all metal was consumed (typically within 2 h). The resulting light yellow solution was filtered and concentrated under vacuum to 10 mL. Then, hexane (10–20 mL) was added, forming a layer over the solution, which was left to crystallize at room temperature. After a few hours, colorless crystals of **1″** were collected, washed with *n*-hexane (3×5 mL), and dried under vacuum. The filtrate was concentrated to 5 mL and produced a crystalline material after standing overnight.

$[Sr_4Zr_2(\mu_6\text{-}O)(\mu_3,\eta^2\text{-}OR)_8(OR)_2(HOR)_4Cl_4]$ (2): A Schlenk flask was charged with $[Cp_2ZrCl_2]$ (1.00 g, 3.42 mmol), Sr metal (0.81 g, 9.24 mmol), 2-methoxyethanol (20 mL, 19.30 g, 0.25 mol), and toluene (20 mL). The mixture was vigorously stirred until all metal was consumed (typically within 5–7 h). The resulting brown solution was filtered and concentrated under vacuum to 20 mL. Hexane (10 mL) was then added, generating a layer over the solution. After 10 d, colorless crystals were collected, washed with *n*-hexane (3× 5 mL), and dried under vacuum. Another portion of crystalline **2** was obtained after one week by layering *n*-hexane over the filtrate. Overall yield: 1.77 g (1.01 mmol, 59%); ^{1}H NMR (500 MHz, $CDCl_3$, 298 K): $\delta=4.23$ (brs; OCH'_2), 4.03 (t, J(H,H)=5 Hz; OCH''_2), 3.80 (brs; CH'_2O), 3.72 (brs; OCH'''_2), 3.70 (s; OCH'_3), 3.49 (brs; CH'''_2O), 3.39 (s; OCH'''_3), 3.37 (m; CH''_2O), 3.27 ppm (s; OCH''_3); $^{13}C\{^1H\}$ NMR (500 MHz, $CDCl_3$, 298 K): $\delta=76.16$, 75.60, 73.69 (CH_2O), 68.02, 65.42, 61.57 (OCH_2), 60.66, 59.09, 58.52 ppm (OCH_3); IR (Nujol): $\tilde{\nu}=$ 3435 (br), 3178 (s), 2925 (vs), 2855 (s), 2717 (w), 1639 (w), 1456 (s), 1377 (m), 1365 (m), 1342 (w), 1251 (w), 1199 (m), 1169 (m), 1159 (m), 1112 (s), 1061 (s), 1023 (s), 965 (w), 903 (m), 836 (m), 701 (s), 565 (s), 466 (s), 426 (s), 390 (m), 333 cm^{-1} (m); elemental analysis calcd (%) for $C_{42}H_{102}O_{29}Cl_4Sr_4Zr_2$: C 28.89, H 5.89, Cl 8.12, Sr 20.07, Zr 10.45; found: C 28.71, H 5.59, Cl 7.99, Sr 19.77, Zr 10.05; GC/MS: CpH, CpH dimer (traces).

$[Ca_4Zr_2(\mu_6\text{-}O)(\mu_3,\eta^2\text{-}OR)_8(OR)_2Cl_4]$ (3): A Schlenk flask was charged with Ca metal (0.277 g, 6.91 mmol), 2-methoxyethanol (20 mL, 19.30 g, 0.25 mol), and toluene (20 mL). The mixture was stirred at 90 °C for 8–12 h for complete consumption of the metal. A solution of $[Cp_2ZrCl_2]$ (1.00 g, 3.42 mmol) in 2-methoxyethanol (10 mL, 9.65 g, 0.125 mol) and toluene (10 mL) were added to the cooled reaction mixture. After 24 h, the dark yellow solution was filtered, and the filtrate was reduced under vacuum to give a powder. *n*-Hexane (50 mL) was added, and the mixture was stirred for 24 h. The precipitate was filtered off, washed with *n*-hexane (2×5 mL), and dried to give **3** as a light brown powder (1.51 g, 1.21 mmol, 71%); ^{1}H NMR (500 MHz, $CDCl_3$, 298 K): $\delta=4.18$ (brs; OCH''_2), 3.77 (brs; OCH'_2), 3.62 (brs; CH''_2O); 3.53 (brs; CH'_2O), 3.48 (s; OCH''_3), 3.44 ppm (s; OCH'_3); $^{13}C\{^1H\}$ NMR (500 MHz, $CDCl_3$, 298 K): $\delta=$

76.01, 73.45 (CH_2O), 64.61, 60.82 (OCH_2), 59.75, 59.49 ppm (OCH_3); IR (Nujol): $\tilde{\nu}$ = 2925 (vs), 2855 (s), 1458 (m), 1377 (w), 1361 (w), 1239 (w), 1196 (w), 1121 (m), 1074 (s), 1015 (w), 980 (vw), 919 (w), 897 (w), 833 (w), 722 (m), 670 (m), 580 (m), 463 (m), 430 (m), 408 (m), 339 cm^{-1} (w); elemental analysis calcd (%) for $C_{30}H_{70}O_{21}Cl_4Ca_4Zr_2$: C 28.79, H 5.64, Cl 11.33, Ca 12.81, Zr 14.58; found: C 29.80, H 6.04, Cl 11.55, Ca 12.30, Zr 14.14; GC/MS: CpH, CpH dimer (traces).

$[Ca_6Zr_2(\mu_2,\eta^2\text{-}OR)_{12}(\mu\text{-}Cl)_2(\eta^2\text{-}HOR)_4Cl_6]\cdot 8\,CH_2Cl_2$ (4·8 CH_2Cl_2): A Schlenk flask was charged with [Cp_2ZrCl_2] (1.00 g, 3.42 mmol), Ca metal (0.21 g, 5.24 mmol), 2-methoxyethanol (20 mL, 19.30 g, 0.25 mol), and toluene (20 mL). The mixture was stirred at 90 °C for 6–10 h for complete consumption of the metal. The resulting light yellow solution was concentrated under vacuum until all the solvents were evaporated. CH_2Cl_2 (15 mL) was then added to the brown viscous material and stirred. The solid did not dissolve immediately, but after about 30 min, a clear light brown solution was observed, which was then concentrated to 5–10 mL. After standing for a few weeks at room temperature, a small amount of white precipitate settled down and **4**·8CH_2Cl_2 was collected as colorless cuboidal crystals, which were then washed with *n*-hexane (3× 5 mL) and dried under vacuum. Overall yield: 0.40 g (0.21 mmol; 24%); ^{1}H NMR (500 MHz, $CDCl_3$, 298 K): δ = 5.30 (s, OH″), 4.45 (m, OCH″$_2$), 3.76 (br s, OCH′$_2$), 3.65 (m, CH″$_2$O), 3.53 (t, CH′$_2$O, J(H,H) = 5 Hz), 3.43 (s, OCH′$_3$), 3.40 (s, OCH″$_3$); ^{13}C{^{1}H} NMR (500 MHz, $CDCl_3$, 298 K): δ = 76.07, 73.40 (CH_2O), 64.68, 60.73 (OCH_2), 59.82, 59.73 ppm (OCH_3); IR (Nujol): $\tilde{\nu}$ = 2927 (vs), 2851 (s), 1460 (m), 1377 (w), 1366 (w), 1234 (w), 1199 (w), 1120 (m), 1070 (s), 1019 (w), 983 (vw), 924 (w), 897 (w), 835 (w), 722 (m), 582 (m), 462 (m), 435 (m), 403 (m), 342 cm^{-1} (w); elemental analysis calcd (%) for $C_{48}H_{116}O_{32}Cl_8Ca_6Zr_2$: C 30.15, H 6.16, Cl 14.83, Ca 12.58, Zr 9.54; found: C, 30.07; H, 6.08; Cl, 14.80; Ca, 12.24; Zr, 9.91; GC/MS: CpH, CpH dimer (traces).

Compounds **1–4** were isolated as thermally stable, air- and moisture-sensitive white solids that are soluble in toluene, alcohols, and chlorinated hydrocarbons at room temperature.

Preparation of barium, strontium, and calcium zirconates: In a typical procedure, $BaZrO_3$ and $SrZrO_3$ were obtained by thermal decomposition of complexes **1** and **2** at 900 and 850 °C, respectively, for 1 h under air at a heating rate of 10 °C min^{-1}. The raw powders were leached with deionized water and dried in an oven at 120 °C for 1 h. The crystal structures of pure barium zirconate and strontium zirconate were evaluated by XRD. In contrast, the molecular precursors **3** and **4** of calcium zirconates were heated at 750 °C for 1 h under air atmosphere at a heating rate of 10 °C min^{-1}. Following decomposition, the raw powders were leached with deionized water. Because elemental analysis of the white powder obtained after decomposition of **3** revealed the presence of C and H contaminants, it was subsequently heat-treated at 900 °C under the same conditions as before. XRD analysis of the final residue confirmed the presence of pure microcrystalline $CaZrO_3$. In the case of **4**, we were unable to obtain highly phase pure oxide material using the above procedures. The morphology and chemical composition of the microcrystalline perovskite zirconates were investigated by TEM-EDS and SEM-EDS. Carbon, hydrogen, and chlorine contaminations were examined by elemental analysis and FTIR spectroscopy.

Preparation of Eu-doped $MZrO_3$ (M = Ba, Sr, Ca): Eu-doped samples were synthesized by mixing $MZrO_3$ (M = Ba, Sr, Ca) derived from **1**, **2**, and **3**, respectively, with Eu_2O_3 and grinding in an alumina mortar with acetone as wetting medium. The resulting raw powders of $MZrO_3$:Eu^{3+} (M = Ba, Sr, Ca) were sintered at 1100 °C in air. The Eu concentration was 3 mol% with respect to Zr.

Acknowledgements

The authors acknowledge the National Science Centre, Poland (Grant No. 2014/13/B/ST5/01512) for financial support.

Keywords: alkaline earth metals · doping · luminescence · O ligands · perovskites

[1] L. Bi, E. Traversa, *J. Mater. Res.* **2014**, *29*, 1–15.
[2] R. Pazik, R. Tekoriute, S. Håkansson, R. Wiglusz, W. Stręk, G. A. Seisenbaeva, Y. K. Gun′ko, V. G. Kessler, *Chem. Eur. J.* **2009**, *15*, 6820–6826.
[3] J. A. Enterkin, W. Setthapun, J. W. Elam, S. T. Christensen, F. A. Rabuffetti, L. D. Marks, P. C. Stair, K. R. Poeppelmeier, C. L. Marshall, *ACS Catal.* **2011**, *1*, 629–635.
[4] C. Moon, M. Nishi, K. Miura, K. Hirao, *J. Lumin.* **2009**, *129*, 817–819.
[5] D. Jia, R. S. Meltzer, W. M. Yen, W. Jia, X. Wang, *Appl. Phys. Lett.* **2002**, *80*, 1535–1537.
[6] R. Borja-Urby, L. A. Diaz-Torres, P. Salas, M. Vega-Gonzalez, C. Angeles-Chavez, *Mater. Sci. Eng. B* **2010**, *174*, 169–173.
[7] L. Guan, L. Jin, S. Guo, Y. Liu, X. Li, Q. Guo, Z. Yang, G. Fu, *J. Rare Earths* **2010**, *28*, 292–294.
[8] J. Huang, L. Zhou, Z. Wang, Y. Lan, Z. Tong, F. Gong, J. Sun, L. Li, *J. Alloys Comp.* **2009**, *487*, 420.
[9] H. Zhang, X. Fu, S. Niu, Q. Xin, *J. Alloys Comp.* **2008**, *459*, 103–106.
[10] X. Li, L. Guan, J.-Y. An, L.-T. Jin, Z.-P. Yang, Y.-M. Yang, P.-L. Li, G.-S. Fu, *Chin. Phys. Lett.* **2011**, *28*, 027805.
[11] J. Huang, L. Zhou, Y. Lan, F. Gong, Q. Li, J. Sun, *Cent. Eur. J. Phys.* **2011**, *9*, 975–979.
[12] S. Szafert, Ł. John, P. Sobota, *Dalton Trans.* **2008**, 6509–6520.
[13] P. Sobota, A. Drąg-Jarząbek, Ł. John, J. Utko, L. B. Jerzykiewicz, M. Duczmal, *Inorg. Chem.* **2009**, *48*, 6584–6593.
[14] P. Sobota, J. Utko, Ł. John, L. B. Jerzykiewicz, A. Drąg-Jarząbek, *Inorg. Chem.* **2008**, *47*, 7939–7941.
[15] Ł. John, P. Sobota, *Acc. Chem. Res.* **2014**, *47*, 470–481.
[16] A. Drąg-Jarząbek, M. Kosińska, Ł. John, L. B. Jerzykiewicz, P. Sobota, *Chem. Mater.* **2011**, *23*, 4212–4219.
[17] Ł. John, J. Utko, S. Szafert, L. B. Jerzykiewicz, L. Kępiński, P. Sobota, *Chem. Mater.* **2008**, *20*, 4231–4239 and references therein.
[18] G. A. Seisenbaeva, S. Gohil, V. G. Kessler, *J. Mater. Chem.* **2004**, *14*, 3177–3190.
[19] J. Utko, S. Przybylak, L. B. Jerzykiewicz, S. Szafert, P. Sobota, *Chem. Eur. J.* **2003**, *9*, 181–190.
[20] A. Mukherjee, S. Nembenna, T. K. Sen, S. P. Sarish, P. Kr. Ghorai, H. Ott, D. Stalke, S. K. Mandal, H. W. Roesky, *Angew. Chem. Int. Ed.* **2011**, *50*, 3968–3972; *Angew. Chem.* **2011**, *123*, 4054–4058.
[21] a) N. Ya. Turova, E. P. Turevskaya, V. G. Kessler, A. I. Yanovsky, Y. T. Struchkov, *J. Chem. Soc. Chem. Commun.* **1993**, 21–23; b) W. A. Herrmann, N. W. Huber, *Angew. Chem.* **1995**, *107*, 2371–2390; c) R. C. Mehrotra, A. Singh, *Chem. Soc. Rev.* **1996**, *25*, 1–13; d) Ł. John, J. Utko, L. B. Jerzykiewicz, P. Sobota, *Inorg. Chem.* **2005**, *44*, 9131–9133; e) N. Y. Turova, *Russ. Chem. Rev.* **2004**, *73*, 1041–1064.
[22] *Handbook of Inorganic Compounds*, 2nd ed. (Ed.: D. L. Perry), CRC Press, Boca Raton, **2011**.

Received: December 2, 2015
Published online on February 18, 2016